Near-field thermal transport between two identical twisted bilayer graphene sheets separated by a vacuum gap

Fuwei Yang [1,2] and Bai Song [1,3,4,*]

[1]*Beijing Innovation Center for Engineering Science and Advanced Technology, Peking University, Beijing 100871, China*
[2]*Center for Nano and Micro Mechanics, Tsinghua University, Beijing 100084, China*
[3]*Department of Energy and Resources Engineering, Peking University, Beijing 100871, China*
[4]*Department of Advanced Manufacturing and Robotics, Peking University, Beijing 100871, China*

Active control of heat flow is of both fundamental and applied interest in thermal management and energy conversion. Here, we present a fluctuational electrodynamic study of thermal radiation between twisted bilayer graphene (TBLG), motivated by its unusual and highly tunable plasmonic properties. We show that near-field heat flow can vary by more than 10-fold over only a few degrees of twist, and observe a larger variation with increasing chemical potential and decreasing temperature. Further, we identify special angles leading to heat flow extrema, which are dictated by the Drude weight in the intraband optical conductivity of TBLG, and are roughly linear with the chemical potential. As the twist angle decreases, we observe multiband thermal transport due to the increasing role of interband transitions, in analogy to monolayer graphene in a magnetic field. We also briefly discuss the effect of a small angular deviation and a substrate, which are experimentally relevant. Our findings are understood via the surface plasmons in TBLG, and highlight its potential for manipulating radiative heat flow.

I. INTRODUCTION

Radiative heat transfer between closely spaced bodies is primarily mediated by the tunneling of evanescent photons [1–3]. Due to the large density of states in the near field, the energy transfer rate can exceed Stefan-Boltzmann's blackbody limit to far-field radiation by orders of magnitude, especially when various surface modes are populated and coupled [4–10]. Surface modes can also enable quasimonochromatic thermal radiation, in contrast to the broadband Planck spectrum [11]. With electrically and chemically tunable surface plasmon polaritons (SPPs) in the terahertz and midinfrared range, graphene offers great potential for enhancing and manipulating near-field radiative heat transfer (NFRHT) over a wide temperature range [12–30]. To this end, both suspended and supported monolayer graphene have been extensively analyzed. Further, graphene SPPs also offer rich opportunities for harnessing thermal radiation in diverse energy conversion and heat management devices, including thermophotovoltaic cells [31,32], thermal switches [33,34], and rectifiers [35,36].

The magic of monolayer graphene (MLG) in NFRHT ultimately lies in its tunable optical conductivity and nonlocal dielectric function, which originate from its characteristic Dirac-cone electronic band structure [37]. Recently, bilayer graphene has attracted a tremendous amount of attention because a small twist angle between the two layers leads to a variety of moiré patterns, which can substantially alter

the band structure and reveal a range of exotic phenomena including correlated insulators and unconventional superconductivity [38–40]. The low-energy band structure of twisted bilayer graphene (TBLG) can be approximately viewed as two shifted MLG Dirac cones, with the moiré Brillouin zone determined by the shift vector (Fig. 1). In addition to a strong optical response similar to MLG, TBLG features a complex low-energy spectrum with multiple interband peaks that are particularly sensitive to the twist angle [41–46]. Despite its rich and unusual electronic and optical properties, the characteristics and potentials of TBLG in NFRHT remain to be explored.

Here, we focus on the theoretical study of near-field thermal transport between two identical suspended TBLG sheets separated by a vacuum gap within the framework of fluctuational electrodynamics (Fig. 1). We employ the effective continuum model and the linear response theory to calculate the electronic structure and optical response of TBLG, respectively, and show that the photon-mediated heat flow can be substantially controlled via the twist angle. In particular, a small twist around some chemical-potential-dependent special angles can lead to over 10-fold heat transfer enhancement. This twist-induced variation is understood via the Drude weight—a key parameter characterizing the intraband optical response of TBLG—and it increases with increasing chemical potential and decreasing temperature. In addition, we find that as the twist angle decreases, interband transitions become increasingly important, leading to multiband thermal transport similar to MLG in a magnetic field. We then demonstrate the essential role of SPPs in the NFRHT of TBLG, and briefly discuss the effect of a small deviation from the desired twist

---

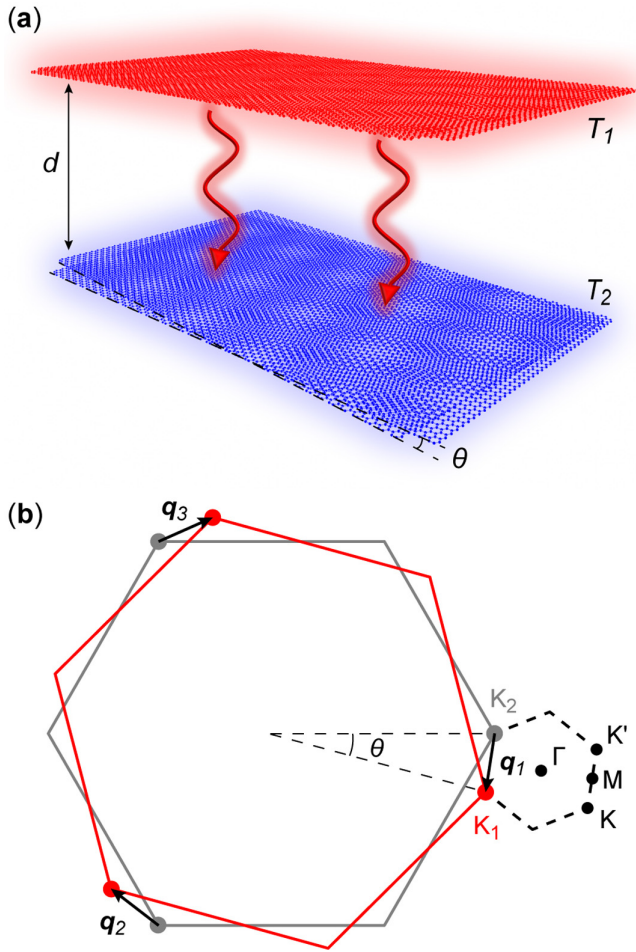*Author to whom all correspondence should be addressed: songbai@pku.edu.cn

(a)

(b)

FIG. 1. (a) Schematic of radiative thermal transport between two identical TBLG sheets separated by a vacuum gap. (b) Reciprocal space of TBLG. The red and gray hexagons represent the first Brillouin zones for the two layers. K_1 and K_2 are the Dirac points. The dashed black hexagon shows the moiré Brillouin zone with the high-symmetry points labeled. $\boldsymbol{q}_j$ represents the nearest-neighbor interlayer hopping process.

angle and that of a substrate, both of which are of experimental importance.

II. METHODS

A. Near-field thermal transport

Based on the theoretical framework of fluctuational electrodynamics, the total heat flux between two parallel planes across a vacuum gap d can be expressed in the Landauer form as [3]

$$q(T_1, T_2, d) = \int_0^\infty d\omega [\Theta(\omega, T_1) - \Theta(\omega, T_2)] f(\omega). \quad (1)$$

Here, $\Theta(\omega, T) = \hbar\omega/[\exp(\hbar\omega/k_B T) - 1]$ is the mean energy of a harmonic oscillator minus the zero-point contribution, and $f(\omega) = \int_0^\infty dk \frac{k}{4\pi^2} [\tau_s(\omega, k) + \tau_p(\omega, k)]$ is the spectral transfer function, with T, ω, and k being the temperature, frequency, and wave-vector component parallel to the planes, respectively. τ_s and τ_p are the photon tunneling probabilities

for the s- and p-polarized waves given by

$$\tau_{\alpha=s,p}^{12}(\omega, k) = \begin{cases} \dfrac{\left(1 - |r_\alpha^1|^2 - |t_\alpha^1|^2\right)\left(1 - |r_\alpha^2|^2 - |t_\alpha^2|^2\right)}{|D_\alpha|^2} & \text{if } k < \omega/c, \\[12pt] \dfrac{4\mathrm{Im}(r_\alpha^1)\mathrm{Im}(r_\alpha^2)e^{-2\mathrm{Im}(\zeta)d}}{|D_\alpha|^2} & \text{if } k > \omega/c, \end{cases} \quad (2)$$

where r_α^i and t_α^i are, respectively, the reflection and transmission coefficients, which for graphene are often written as functions of the optical conductivity [47], $D_\alpha = 1 - r_\alpha^1 r_\alpha^2 e^{2i\zeta d}$ is a Fabry-Pérot-like denominator, and ζ is the transverse wave-vector component. We further define the spectral and total heat transfer coefficient in the linear regime as $h_\omega = \frac{\partial\Theta(\omega, T)}{\partial T} f(\omega)$ and $h = \int_0^\infty d\omega h_\omega$, respectively.

B. Band structure of TBLG

To obtain the optical conductivity of TBLG, we start by calculating its electronic band structure. We focus on the regime of low energy ($\leqslant 1\,\mathrm{eV}$) and small twist angles ($\sim 2°$ to $8°$), which is well described by the widely used effective continuum model [38,43,46,48,49]. The Hamiltonian is usually written as

$$H = \begin{pmatrix} H_1 & U \\ U^\dagger & H_2 \end{pmatrix}, \quad (3)$$

where H_l ($l = 1, 2$) is the Dirac Hamiltonian for the two layers, while U denotes interlayer hopping. Expanding around the Diarc points K_1 and K_2 in Fig. 1(b), H_l can be written as

$$H_l(\boldsymbol{k}) = \hbar v_F (\boldsymbol{k} - \boldsymbol{K}_l) \cdot \boldsymbol{\sigma}. \quad (4)$$

Here, $\boldsymbol{\sigma}$ denotes the Pauli matrices, $v_F = \sqrt{3}a_0 t_0/2\hbar \approx 10^6\,m/s$ is the Fermi velocity, with the graphene lattice constant $a_0 = 2.46\,\text{Å}$ and the intralayer hopping integral t_0 chosen as 2.78 eV. Considering nearest-neighbor coupling only, the interlayer hopping term is given by [38]

$$U = t_\perp \sum_{j=1}^3 \exp(-i\boldsymbol{q}_j \cdot \boldsymbol{r}) U^j, \quad (5)$$

with $U^1 = \begin{pmatrix} 1 & 1 \\ 1 & 1 \end{pmatrix}$, $U^2 = \begin{pmatrix} e^{i\phi} & 1 \\ e^{-i\phi} & e^{i\phi} \end{pmatrix}$, $U^3 = \begin{pmatrix} e^{-i\phi} & 1 \\ e^{i\phi} & e^{-i\phi} \end{pmatrix}$, and $\phi = \frac{2}{3}\pi$. $\boldsymbol{q}_j$ represents interlayer hopping [Fig. 1(b)] with an energy of $t_\perp = 0.11$ eV.

As an example, the calculated band structure and the corresponding density of states (DOS) for TBLG with a twist angle of $3°$ are shown in Fig. 2(a). In the vicinity of the K (K') point, the typical linear dispersion for monolayer graphene remains. However, the band structure becomes rather complex with increasing energy. In particular, the appearance of saddle points due to anticrossing at the band intersections of different layers leads to van Hove singularities followed by steplike singularities (an example is marked by the red dashed line) in the DOS [43,44], which substantially affect the optical transitions in TBLG.

C. Optical conductivity of TBLG

We first compute the real part of the optical conductivity (σ) of TBLG from its band structure via the Kubo formula [43,46]. Subsequently, the imaginary part is obtained through
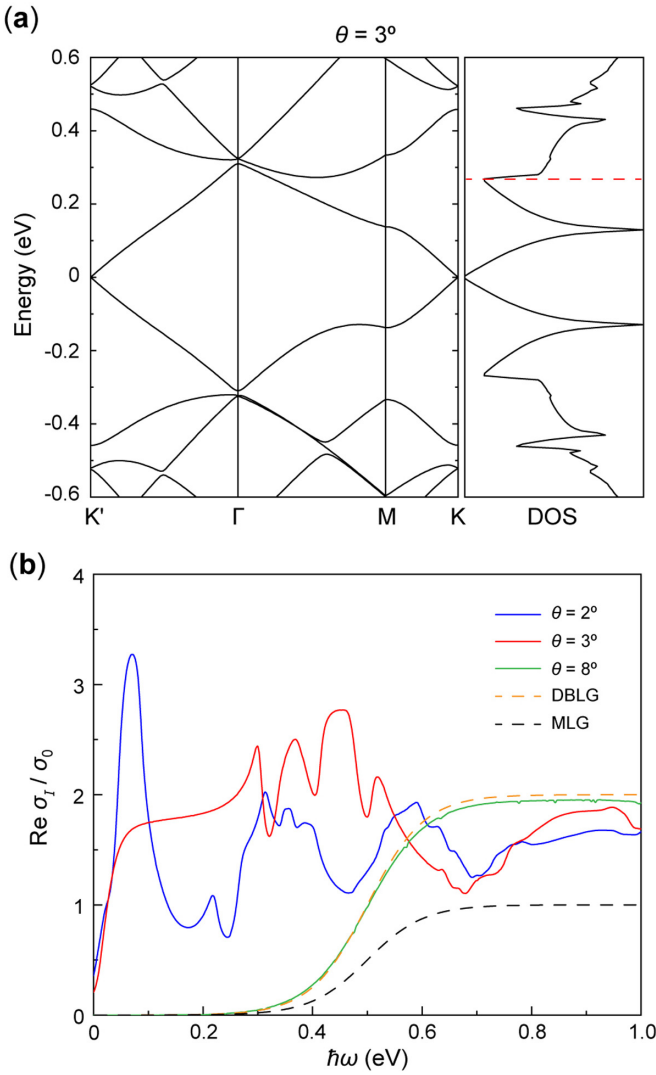
FIG. 2. (a) The calculated electronic band structure and density of states of TBLG with a twist angle of 3°. The red dashed line marks the first steplike singularity away from the charge-neutrality point. (b) Real part of the interband optical conductivity of MLG, DBLG, and TBLG with representative twist angles. $\sigma_0 = e^2/4\hbar$ is the universal conductivity of MLG.

the Kramers-Kronig relation [46]. For graphene, σ is often divided into an intraband (Drude) and an interband term as

$$\sigma(\omega) = \sigma_D + \sigma_I. \qquad (6)$$

The intraband conductivity can be written as

$$\sigma_D(\omega) = \frac{D}{\pi} \frac{i}{\hbar\omega + i\Gamma}, \qquad (7)$$

where Γ represents the electron scattering rate and is chosen as 7 meV, and D is the Drude weight characterizing the strength of intraband transitions [37] and is calculated as [46]

$$D = \frac{4\sigma_0}{\pi\hbar} \int d\boldsymbol{k} \sum_m \left(\frac{\partial \epsilon_{m,\boldsymbol{k}}}{\partial k_x}\right)^2 \frac{\partial n_F(\epsilon_{m,\boldsymbol{k}})}{\partial \epsilon}. \qquad (8)$$

Here, $n_F(\epsilon) = 1/[\exp[(\epsilon-\mu)/k_BT]-1]$ is the Fermi distribution function, μ is the chemical potential, $\epsilon_{m,\boldsymbol{k}}$ is the energy

of the mth band with momentum $\boldsymbol{k}$, and $\sigma_0 = e^2/4\hbar$. The integration is taken over the first moiré Brillouin zone, and only the x-component is considered because of the hexagonal symmetry in TBLG [46]. For the interband conductivity, the real part is calculated as [43]

$$\mathrm{Re}\,\sigma_I(\omega) = \frac{4\sigma_0}{\pi} \int d^2\boldsymbol{k} \sum_{mn} [n_F(\epsilon_{n,\boldsymbol{k}}) - n_F(\epsilon_{m,\boldsymbol{k}})]$$
$$\times |\langle m, \boldsymbol{k}|j_x|n, \boldsymbol{k}\rangle|^2 \frac{\delta(\hbar\omega - \epsilon_{m,\boldsymbol{k}} + \epsilon_{n,\boldsymbol{k}})}{\epsilon_{m,\boldsymbol{k}} - \epsilon_{n,\boldsymbol{k}}}. \qquad (9)$$

Here, $j_x = -\frac{\partial H}{\partial k_x}$ is the current operator, $|n, \boldsymbol{k}\rangle$ represents the eigenstates, and $\delta(x)$ is replaced by $\Gamma/\pi/(x^2 + \Gamma^2)$ in numerical computation.

In Fig. 2(b), we show the calculated optical conductivity at $\mu = 0.25$ eV for MLG, decoupled bilayer graphene (DBLG), and TBLG with $\theta = 2°$, 3° and 8°. Ignoring interlayer coupling, the optical conductivity of DBLG is simply twice that of MLG [46]. At a large twist angle of 8°, the optical conductivity of TBLG approaches that of DBLG with minor differences at relatively high energy. As the twist angle decreases, a series of low-energy peaks appear due to interband transitions, in clear contrast to DBLG. After obtaining the real part of the interband conductivity, the imaginary part is then calculated as [46]

$$\mathrm{Im}\,\sigma_I(\omega) = \frac{2\omega}{\pi}\mathcal{P} \int_0^\infty dv \frac{\mathrm{Re}\,\sigma_I(v) - 2\sigma_0}{\omega^2 - v^2}, \qquad (10)$$

where $\mathcal{P}$ denotes the Cauchy principal integral.

III. RESULTS AND DISCUSSION

A. Twist-angle-sensitive heat flow

The significant effect of the twist angle on NFRHT is first manifested in the total heat transfer coefficient (HTC). In Fig. 3(a), we plot the HTC for MLG, DBLG, and TBLG with $\theta = 8°$, 3°, and 2° at $T = 300$ K, $\mu = 0.25$ eV, and gap sizes from 100 μm to 1 nm. All cases show a dramatic HTC enhancement with reducing gap, eventually exceeding the blackbody limit by over three orders of magnitude. The HTC of TBLG with an 8° twist ($h_{\theta=8°}$) overlaps with that of DBLG (h_{DBLG}), since their optical conductivities converge at very low energy [Fig. 2(b)]. At nanometer gaps, $h_{\theta=8°}$ is roughly half of h_{MLG}. As the twist angle reduces to 3° and further to 2°, the HTC first increases to $\sim 7h_{\mathrm{MLG}}$ (that is, $\sim 14h_{\theta=8°}$) and then drops back to $\sim 3h_{\mathrm{MLG}}$. At micrometer gaps, however, the opposite trend is observed, with $h_{\theta=8°}$ being the largest and $h_{\theta=3°}$ the smallest.

To understand the twist-induced HTC suppression and enhancement, we performed systematic calculations for θ from 1.5° to 8° at two representative gap sizes of $d = 10$ nm and 1 μm [Fig. 3(b)]. At small twist angles, h_{TBLG} clearly forms a peak for the 10 nm gap. Interestingly, for the 1 μm gap, a dip appears instead at about the same twist angle, which is roughly 3° for $\mu = 0.25$ eV. This contrast between small and large gaps is discussed later via the coupling of SPPs in TBLG. As the twist angle increases beyond $\sim 6°$, h_{TBLG} consistently approaches h_{DBLG} regardless of the gap size. For even larger θ, which can be treated with a tight-binding model [44], we
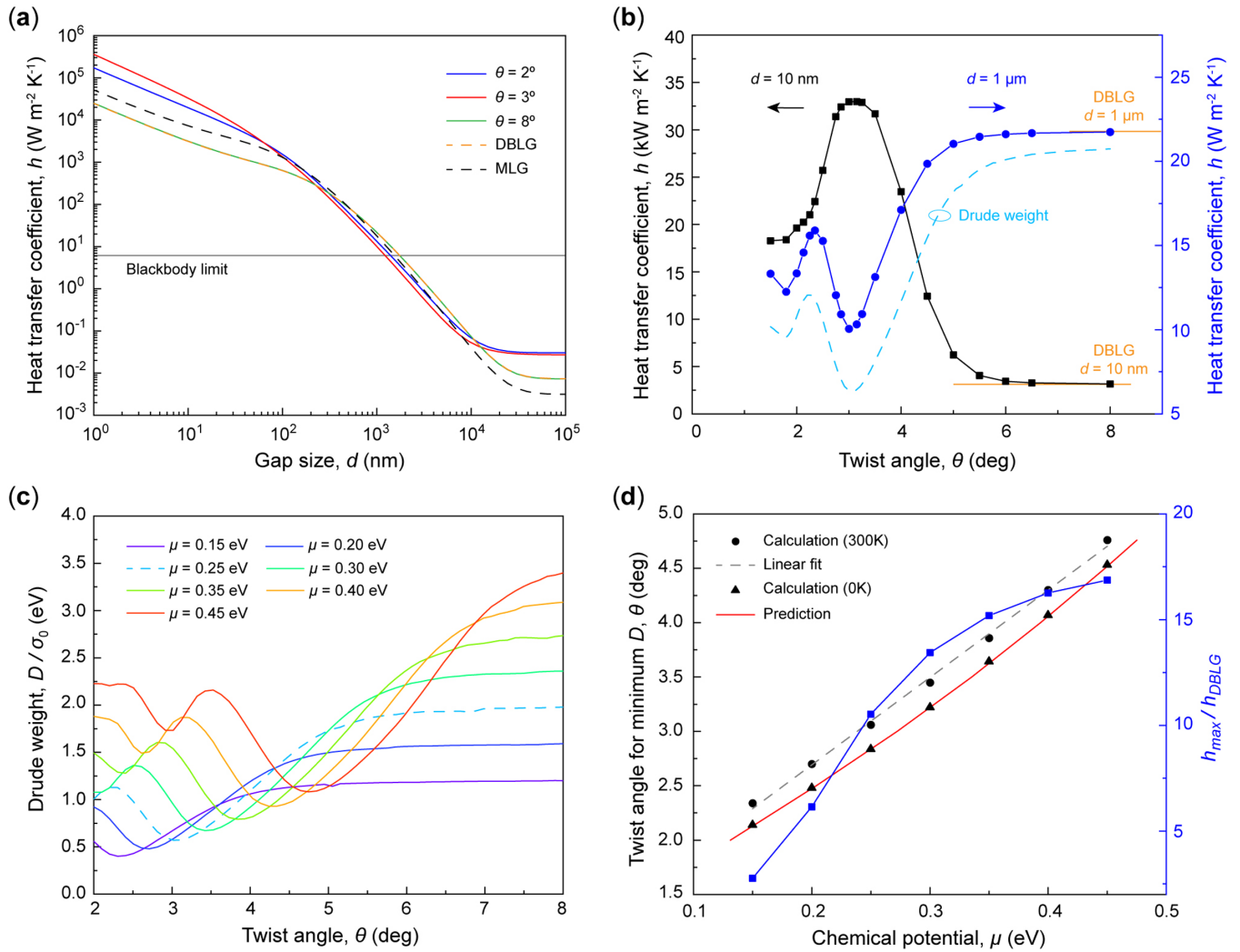
FIG. 3. Twist-angle-dependent NFRHT. (a) Heat transfer coefficient as a function of gap size for representative cases at $T = 300$ K and $\mu = 0.25$ eV. (b) Heat transfer coefficient as a function of twist angle for $d = 10$ nm and $d = 1\,\mu$m. The dashed cyan curve shows the corresponding Drude weight. (c) Variation of Drude weight with twist angle at different chemical potentials. (d) Left: twist angles for minimum Drude weight as a function of chemical potential at $T = 300$ K (black circles) and 0 K (black triangles). The gray dashed line is a linear fit, while the red solid line is the prediction using the DOS. Right: the blue squares show the maximum HTC enhancement at different chemical potentials.

omit an exact calculation but argue that h_{TBLG} should remain close to h_{DBLG} since the optical conductivities only differ at very high energy, which contributes little to heat transfer.

B. Special angle identification via the Drude weight

Our results above demonstrate that it is possible to tune the near-field radiative heat flow by over 10-fold with only a few degrees of twist around some special angle. In Fig. 3(b), we show that at $\mu = 0.25$ eV, the special angle for the maximum (10 nm gap) and minimum (1 μm gap) of h_{TBLG} is also where the Drude weight reaches its first minimum as the twist angle decreases. Such an observation holds at other chemical potentials (see [47] for $\mu = 0.15$ and 0.35 eV) as well, suggesting that the Drude weight can be used to quickly identify special angles for heat flow extrema without actually computing NFRHT, which demands the resource-intensive computation

of the full conductivity. The reason that the Drude weight can be a good indicator of the heat flow is twofold. First, the Drude conductivity dominates at low energy except for twist angles about or below 2°. Secondly, only low-energy optical responses matter in NFRHT near room temperature.

In Fig. 3(c), we plot the Drude weight as a function of θ for a range of chemical potentials from 0.15 to 0.45 eV at $T = 300$ K. By extracting the largest twist angle where the Drude weight is a minimum in each case [black circles in Fig. 3(d)], we observe an approximately linear relation between the special angle and the chemical potential, which offers a convenient way to identify these angles. We further explore the physical origin of the special angle in light of the correspondence between the peaks and dips in the Drude weight and those in the DOS [43]. In particular, we speculate that the special angle arises from the match between the energy of the first DOS minimum [red line in Fig. 2(a)]

and a given chemical potential, as the twist angle varies. This understanding is validated by the overlap between the special angles computed from the Drude weight at $T = 0$ K [to eliminate the small temperature-induced shift at $T = 300$ K, black triangles in Fig. 3(d)] and those predicted via the DOS (red line). Our calculation also confirms that the linear relation between the special angle and the chemical potential is only an approximation, which holds reasonably well in the energy range of interest.

In addition to the scaling of the special angle with the chemical potential, we notice in Fig. 3(c) that the ratio between the maximum and minimum Drude weight increases with increasing chemical potential, which suggests that the HTC may exhibit a similar behavior. Indeed, the ratio of h_{max} (calculated at the special angles) to h_{DBLG} is larger at larger μ, as shown by the blue squares in Fig. 3(d). We note that h_{max}/h_{DBLG} also increases with decreasing temperature (Fig. S2 [47]) due to the thermal smearing of the variations in Drude weight [43,46]. Despite the observation of an approximate correspondence between the Drude weight and the heat flow at relatively large angles, we also notice a clear deviation at small gaps for twist angles $\lesssim 2°$ [Fig. 3(b)], which signifies an increasing influence of the interband transitions.

C. Multiband transport at small twist angles

Motivated by the appearance of multiple low-energy peaks in the optical conductivity with decreasing twist angle [Fig. 2(b)], we now explore the spectral characteristics of NFRHT in TBLG. To this end, we compare TBLG with $\theta = 2°$ to DBLG at $\mu = 0$ eV, $d = 10$ nm, and $T = 300, 600,$ and 1000 K. The spectral heat transfer coefficient of DBLG [Fig. 4(a)] features a single peak at all three temperatures. The spectral HTC of TBLG also shows a single peak (with a small shoulder) at room temperature; however, as temperature increases, an increasing number of peaks become visible. These multiband transport spectra apparently arise from the interband transitions, with the temperature serving as an energy filter through the Boltzmann factor $\Theta(\omega, T)$.

To further explore the underlying mechanism, we focus on the spectral transfer function so that the temperature factor is dropped. We first note that f_{TBLG} almost overlaps with f_{DBLG} at the lowest energies where Drude conductivity dominates. More interestingly, f_{TBLG} ($\theta = 2°$) exhibits multiple peaks and dips absent in f_{DBLG}, whose positions coincide with those in the imaginary part of the optical conductivity [Fig. 4(c)]. Specifically, f_{TBLG} drops sharply whenever Im σ becomes negative, which leads to optical gaps where SPPs can no longer be sustained [37,43]. Similarly, these oscillations of Im σ around 0 also underlie the multiband transport predicted for MLG in a moderately strong magnetic field on the order of 1 T and at low chemical potentials [50,51], although the latter originates from interband transitions between the regularly spaced Landau levels. The above results suggest that TBLG can also be used to control the radiation spectrum.

D. Surface plasmon polaritons in TBLG

To gain a deeper insight into the unique characteristics of TBLG in NFRHT, we analyze the photon tunneling proba-
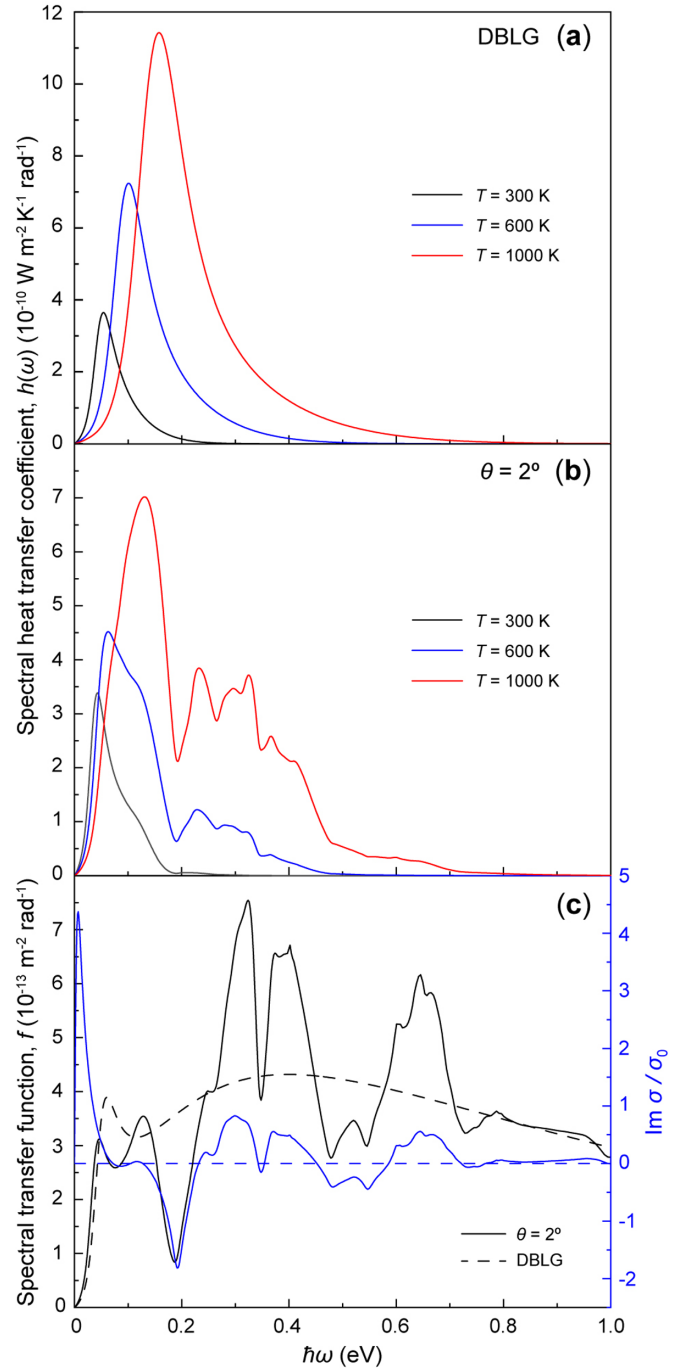

FIG. 4. Multiband transport in TBLG. Spectral heat transfer coefficient for (a) DBLG and (b) TBLG with $\theta = 2°$ at room and higher temperatures, with $\mu = 0$ eV and $d = 10$ nm. (c) The spectral transfer function (left) for DBLG and TBLG with $\theta = 2°$, and the imaginary part of the optical conductivity of TBLG (right). The dashed blue line indicates Im $\sigma = 0$.

bility and highlight the contributions of p-polarized surface plasmon polaritons. As in the case of MLG, the s-polarized waves contribute negligibly [47]. In Fig. 5, we present τ_p for MLG and TBLG with $\theta = 8°, 3°,$ and $2°$ at $\mu = 0.25$ eV and $d = 10$ nm. In addition, we calculate the dispersion relations of the coupled SPPs by setting $D_p = 1 - r_p^1 r_p^2 e^{2i\zeta d} = 0$,
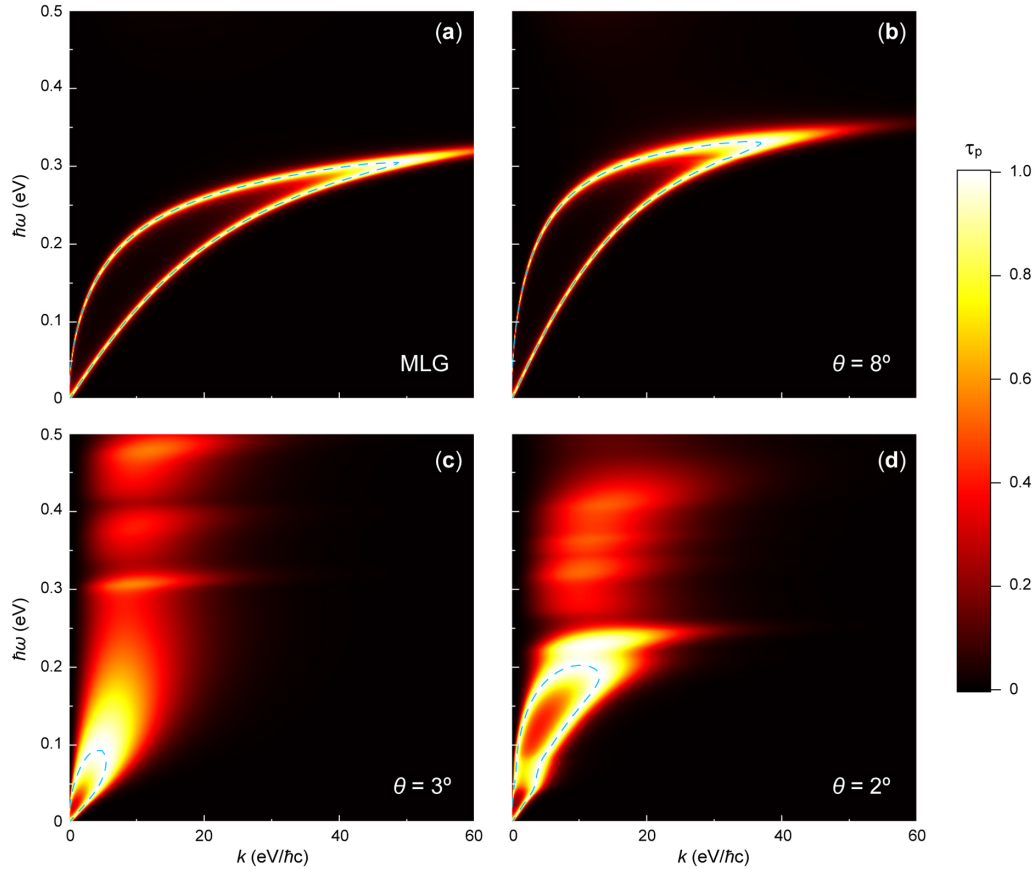
FIG. 5. Photon tunneling probability τ_p across a 10 nm gap at $\mu = 0.25$ eV. (a) MLG. (b)–(d) TBLG with $\theta = 8°$, $3°$, and $2°$, respectively. The dashed cyan lines represent the dispersions of coupled SPPs.

and we plot them on top of the τ_p maps. The overlap between the dispersion curves and the peaks of τ_p confirms that the coupled SPPs are the dominant mediator for the large near-field HTC of TBLG [7]. For $\theta = 8°$, the dispersion curve [Fig. 5(b)] is similar to that of MLG [Fig. 5(a)], with well-defined acoustic and optical branches merging at sufficiently large wave vectors [37]. Compared to h_{MLG}, the smaller $h_{\theta=8°}$ (Fig. 3) is due to a shift of the mode-merging region to higher energy and lower wave vector. We note that this shift results from an increase in the Drude weight, since the slope of the intraband plasmon dispersion scales as $\sqrt{D}$ [37,43].

At the smaller twist angles of $3°$ and $2°$ [Figs. 5(c) and 5(d)], the dispersions noticeably deviate from that of MLG as a result of a growing influence of interband transitions on the intraband plasmons, which explains the lack of correspondence between the Drude weight and the HTC at small angles [Fig. 3(b)]. In addition, multiple high-transmission regions appear which are absent in MLG, and they shift to lower energy as θ decreases. These regions represent contributions from the unconventional interband plasmons described in previous work [43], which together with the gaps in-between result in the multiband transport in TBLG.

In general, the above discussions are valid for nanometer gaps. As the gap size increases, the attenuation of SPPs limits any effective coupling to smaller wave vectors where intraband transitions become even more dominant. For intra-

band plasmons, the attenuation length is proportional to the Drude weight [37]. Therefore, a larger Drude weight leads to stronger coupling and thus higher HTC at sufficiently large gaps, contrary to the case of small gaps [Fig. 3(b)].

E. Robustness against angular deviation and the influence of substrate

In addition to our focus on the basic characteristics of NFRHT between two identical suspended TBLG sheets, we briefly discuss some realistic factors concerning potential experimental study, including the effect of an angular deviation or a substrate. In practice, preparing a TBLG sheet with exactly the desired twist angle is undoubtedly challenging. However, recent technological development has already demonstrated the possibility of controlling the twist angle with a high accuracy of $0.1°$ [52–54]. To find out how such a small angular deviation could affect NFRHT, we consider a case with the top TBLG sheet deviating from the nominal twist angle θ by $0.25°$ while the bottom one deviates by $-0.25°$, which is a total of $0.5°$. In Fig. 6(a), we plot the HTC as a function of θ at a gap size of 10 nm with $\mu = 0.25$ eV and $T = 300$ K, which shows a dramatic variation quantitatively similar to the ideal case of two identical sheets. This suggests that state-of-the-art TBLG preparation techniques are ready for the experimental study of NFRHT.
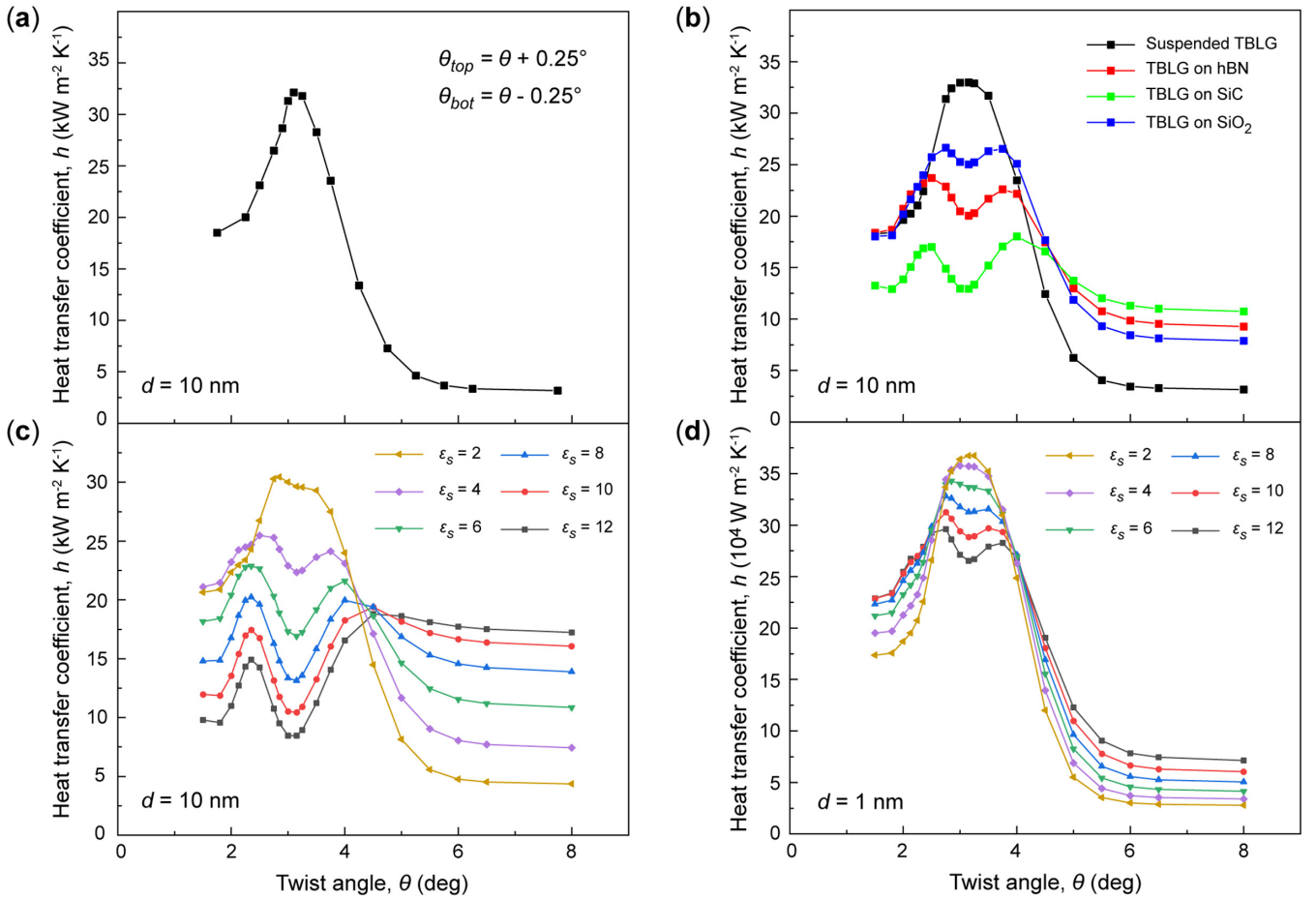
FIG. 6. The effects of a small angular deviation and a substrate, with $T = 300$ K and $\mu = 0.25$ eV. (a) The twist angles of the two TBLG sheets deviate from the nominal value by $\pm 0.25°$, respectively. (b) The effect of a bulk hBN, SiC, or SiO$_2$ substrate. The black curve is taken from Fig. 3(b) as a convenient reference. The substrate permittivities are found in Refs. [1,7,24]. (c) and (d) The effect of an imaginary substrate with a constant permittivity ε_s.

Similar to MLG, suspended TBLG can be prepared over a TEM grid or a tailored microstructure [55–57]. However, substrate-supported TBLG can often come in handy in an experiment. To briefly look into the substrate effect, we first consider hexagonal boron nitride (hBN), silicon carbide (SiC), and silicon dioxide (SiO$_2$), which represent some of the most widely used materials in TBLG devices and NFRHT measurement. In Fig. 6(b), we plot the HTC between supported TBLG at $d = 10$ nm, $\mu = 0.25$ eV, and $T = 300$ K. Despite large differences in their dielectric responses, all three substrates reduce the contrast between the maximum and minimum HTC. In addition, the peak around the special angle for suspended TBLG now becomes a dip. To understand these effects, we consider the simplified case with a substrate of constant permittivity ε_s. As shown in Fig. 6(c), the HTC contrast at $d = 10$ nm reduces as ε_s increases while the peak gradually turns into a dip, similar to our observation with the real substrates. We propose that such variations can be attributed to the attenuation length of the graphene SPPs, which is inversely proportional to ε_s [37]. As a result, increasing ε_s reduces the coupling between the two TBLG sheets, similar

to increasing the gap size. Indeed, a much smaller substrate effect is seen at a smaller gap of 1 nm [Fig. 6(d)].

IV. CONCLUSION

In summary, we theoretically demonstrate that near-field radiative thermal transport between two suspended twisted bilayer graphene sheets can be effectively controlled by the twist angle. In terms of heat flow, we observe over 10-fold variation as the twist angle varies by only a few degrees around some special angle, which is dictated by the Drude weight that characterizes the intraband plasmons of TBLG, and scales approximately linearly with the chemical potential. The twist-induced heat flow variation increases with increasing chemical potential and decreasing temperature. In addition, multiband thermal transport occurs at sufficiently small twist angles, as the interband plasmons become increasingly important. We also briefly discuss the effects of a substrate and a small angular deviation considering their experimental relevance.

Our current investigation is limited to chemical potentials below 0.45 eV and twist angles from 1.5° to 8°. For smaller twist angles approaching the first magic angle, lattice relaxation becomes non-negligible [58–60], which represents the topic of an ongoing study. Another aspect of potential interest for NFRHT is the chiral response of TBLG, which is only captured when the finite separation and the dephasing of the electric field between the two layers are modeled [61–63]. Our results offer a way to control radiative heat flow, and open yet another avenue for uncovering the full potential of the twist degree of freedom in graphene and similar materials.

[1] K. Joulain, J.-P. Mulet, F. Marquier, R. Carminati, and J.-J. Greffet, Surf. Sci. Rep. **57**, 59 (2005).

[2] X. Liu, L. Wang, and Z. M. Zhang, Nanoscale Microscale Thermophys. Eng. **19**, 98 (2015).

[3] B. Song, A. Fiorino, E. Meyhofer, and P. Reddy, AIP Adv. **5**, 053503 (2015).

[4] J. P. Mulet, K. Joulain, R. Carminati, and J. J. Greffet, Microscale Thermophys. Eng. **6**, 209 (2002).

[5] S. Shen, A. Narayanaswamy, and G. Chen, Nano Lett. **9**, 2909 (2009).

[6] E. Rousseau, A. Siria, G. Jourdan, S. Volz, F. Comin, J. Chevrier, and J. J. Greffet, Nat. Photon. **3**, 514 (2009).

[7] B. Song, Y. Ganjeh, S. Sadat, D. Thompson, A. Fiorino, V. Fernández-Hurtado, J. Feist, F. J. Garcia-Vidal, J. C. Cuevas, P. Reddy, and E. Meyhofer, Nat. Nanotechnol. **10**, 253 (2015).

[8] K. Kim, B. Song, V. Fernandez-Hurtado, W. Lee, W. Jeong, L. Cui, D. Thompson, J. Feist, M. T. H. Reid, F. J. Garcia-Vidal, J. C. Cuevas, E. Meyhofer, and P. Reddy, Nature **528**, 387 (2015).

[9] B. Song, D. Thompson, A. Fiorino, Y. Ganjeh, P. Reddy, and E. Meyhofer, Nat. Nanotechnol. **11**, 509 (2016).

[10] A. Fiorino, D. Thompson, L. Zhu, B. Song, P. Reddy, and E. Meyhofer, Nano Lett. **18**, 3711 (2018).

[11] J. J. Greffet, R. Carminati, K. Joulain, J. P. Mulet, S. P. Mainguy, and Y. Chen, Nature **416**, 61 (2002).

[12] A. I. Volokitin and B. N. J. Persson, Phys. Rev. B **83**, 241407(R) (2011).

[13] O. Ilic, M. Jablan, J. D. Joannopoulos, I. Celanovic, H. Buljan, and M. Soljačić, Phys. Rev. B **85**, 155422 (2012).

[14] V. B. Svetovoy, P. J. van Zwol, and J. Chevrier, Phys. Rev. B **85**, 155418 (2012).

[15] P. J. van Zwol, S. Thiele, C. Berger, W. A. de Heer, and J. Chevrier, Phys. Rev. Lett. **109**, 264301 (2012).

[16] M. Lim, S. S. Lee, and B. J. Lee, Opt. Express **21**, 22173 (2013).

[17] X. Liu, R. Z. Zhang, and Z. Zhang, ACS Photon. **1**, 785 (2014).

[18] P. Ben-Abdallah, A. Belarouci, L. Frechette, and S. A. Biehs, Appl. Phys. Lett. **107**, 053109 (2015).

[19] P. Rodriguez-Lopez, W. K. Tse, and D. A. Dalvit, J. Phys. Condens. Matter **27**, 214019 (2015).

[20] J.-H. Jiang and J.-S. Wang, Phys. Rev. B **96**, 155437 (2017).

[21] R. Yu, A. Manjavacas, and F. J. García de Abajo, Nat. Commun. **8**, 2 (2017).

[22] K. Shi, F. Bao, and S. He, ACS Photon. **4**, 971 (2017).

[23] R. Messina, P. Ben-Abdallah, B. Guizal, and M. Antezza, Phys. Rev. B **96**, 045402 (2017).

[24] B. Zhao, B. Guizal, Z. M. Zhang, S. Fan, and M. Antezza, Phys. Rev. B **95**, 245437 (2017).

[25] F. V. Ramirez, S. Shen, and A. J. H. McGaughey, Phys. Rev. B **96**, 165427 (2017).

[26] J. Yang, W. Du, Y. Su, Y. Fu, S. Gong, S. He, and Y. Ma, Nat. Commun. **9**, 4033 (2018).

[27] N. H. Thomas, M. C. Sherrott, J. Broulliet, H. A. Atwater, and A. J. Minnich, Nano Lett. **19**, 3898 (2019).

[28] K. Shi, Y. Sun, Z. Chen, N. He, F. Bao, J. Evans, and S. He, Nano Lett. **19**, 8082 (2019).

[29] X. Ying and A. Kamenev, Phys. Rev. B **102**, 195426 (2020).

[30] C.-L. Zhou, L. Qu, Y. Zhang, and H.-L. Yi, Phys. Rev. B **102**, 245421 (2020).

[31] O. Ilic, M. Jablan, J. D. Joannopoulos, I. Celanovic, and M. Soljačić, Opt. Express **20**, A366 (2012).

[32] V. B. Svetovoy and G. Palasantzas, Phys. Rev. Appl. **2**, 034006 (2014).

[33] O. Ilic, N. H. Thomas, T. Christensen, M. C. Sherrott, M. Soljacic, A. J. Minnich, O. D. Miller, and H. A. Atwater, ACS Nano **12**, 2474 (2018).

[34] G. T. Papadakis, B. Zhao, S. Buddhiraju, and S. Fan, ACS Photon. **6**, 709 (2019).

[35] Z. Zheng, X. Liu, A. Wang, and Y. Xuan, Int. J. Heat Mass Transf. **109**, 63 (2017).

[36] G. Xu, J. Sun, H. Mao, and T. Pan, J. Appl. Phys. **124**, 183104 (2018).

[37] P. A. D. Gonçalves and N. M. R. Peres, *An Introduction to Graphene Plasmonics* (World Scientific, Singapore, 2016).

[38] R. Bistritzer and A. H. MacDonald, Proc. Natl. Acad. Sci. (U.S.A.) **108**, 12233 (2011).

[39] Y. Cao, V. Fatemi, A. Demir, S. Fang, S. L. Tomarken, J. Y. Luo, J. D. Sanchez-Yamagishi, K. Watanabe, T. Taniguchi, E. Kaxiras, R. C. Ashoori, and P. Jarillo-Herrero, Nature **556**, 80 (2018).

[40] Y. Cao, V. Fatemi, S. Fang, K. Watanabe, T. Taniguchi, E. Kaxiras, and P. Jarillo-Herrero, Nature **556**, 43 (2018).

[41] X. Zou, J. Shang, J. Leaw, Z. Luo, L. Luo, C. La-o-vorakiat, L. Cheng, S. A. Cheong, H. Su, J.-X. Zhu, Y. Liu, K. P. Loh, A. H. Castro Neto, T. Yu, and E. E. M. Chia, Phys. Rev. Lett. **110**, 067401 (2013).

[42] C. J. Tabert and E. J. Nicol, Phys. Rev. B **87**, 121402(R) (2013).

[43] T. Stauber, P. San-Jose, and L. Brey, New J. Phys. **15**, 113050 (2013).

[44] P. Moon and M. Koshino, Phys. Rev. B **87**, 205404 (2013).

[45] K. Yu, N. Van Luan, T. Kim, J. Jeon, J. Kim, P. Moon, Y. H. Lee, and E. J. Choi, Phys. Rev. B **99**, 241405(R) (2019).

[46] G. Catarina, B. Amorim, E. V. Castro, J. M. V. P. Lopes, and N. Peres, in *Handbook of Graphene Set*, edited by E. Celasco, A. N. Chaika, T. Stauber, M. Zhang, C. Ozkan, U. Ozkan, B. Palys, and S. W. Harun (Wiley, New Jersey, 2019), pp. 177.

[47] See Supplemental Material at http://link.aps.org/supplemental/10.1103/PhysRevB.103.235415 for expressions of the reflection and transmission coefficients, the HTC at additional chemical potentials, the variation of the maximum HTC contrast with temperature, and a comparison of contributions from s- and p-polarized waves.

[48] J. M. Lopes dos Santos, N. M. R. Peres, and A. H. Castro Neto, Phys. Rev. Lett. **99**, 256802 (2007).

[49] J. M. B. Lopes dos Santos, N. M. R. Peres, and A. H. Castro Neto, Phys. Rev. B **86**, 155449 (2012).

[50] L. Ge, K. Gong, Y. Cang, Y. Luo, X. Shi, and Y. Wu, Phys. Rev. B **100**, 035414 (2019).

[51] H. Wu, Y. Huang, L. Cui, and K. Zhu, Phys. Rev. Appl. **11**, 054020 (2019).

[52] X. D. Chen, W. Xin, W. S. Jiang, Z. B. Liu, Y. Chen, and J. G. Tian, Adv. Mater. **28**, 2563 (2016).

[53] K. Kim, M. Yankowitz, B. Fallahazad, S. Kang, H. C. Movva, S. Huang, S. Larentis, C. M. Corbet, T. Taniguchi, K. Watanabe, S. K. Banerjee, B. J. LeRoy, and E. Tutuc, Nano Lett. **16**, 1989 (2016).

[54] L. Cai and G. Yu, Adv. Mater. **33**, e2004974 (2021).

[55] A. A. Balandin, S. Ghosh, W. Bao, I. Calizo, D. Teweldebrhan, F. Miao, and C. N. Lau, Nano Lett. **8**, 902 (2008).

[56] H. Li, H. Ying, X. Chen, D. L. Nika, A. I. Cocemasov, W. Cai, A. A. Balandin, and S. Chen, Nanoscale **6**, 13402 (2014).

[57] Y. Hou, X. Ren, J. Fan, G. Wang, Z. Dai, C. Jin, W. Wang, Y. Zhu, S. Zhang, L. Liu, and Z. Zhang, ACS Appl. Mater. Interfaces **12**, 40958 (2020).

[58] N. N. T. Nam and M. Koshino, Phys. Rev. B **96**, 075311 (2017).

[59] M. Koshino, N. F. Q. Yuan, T. Koretsune, M. Ochi, K. Kuroki, and L. Fu, Phys. Rev. X **8**, 031087 (2018).

[60] S. Carr, S. Fang, Z. Zhu, and E. Kaxiras, Phys. Rev. Res. **1**, 013001 (2019).

[61] E. Suárez Morell, L. Chico, and L. Brey, 2D Mater. **4**, 035015 (2017).

[62] T. Stauber, T. Low, and G. Gomez-Santos, Phys. Rev. Lett. **120**, 046801 (2018).

[63] X. Lin, Z. Liu, T. Stauber, G. Gomez-Santos, F. Gao, H. Chen, B. Zhang, and T. Low, Phys. Rev. Lett. **125**, 077401 (2020).